THE EFFECT OF THE pH VALUES AND SINTERING TEMPERATURES ON THE PHYSICAL, STRUCTURAL AND MECHANICAL PROPERTIES OF NANO HYDROXYAPATITE DERIVED FROM ARK CLAM SHELLS (*ANADARA GRANOSA*) PREPARED VIA THE WET CHEMICAL PRECIPITATE METHOD

MOHAMMAD ZULHASIF AHMAD KHIRI*, #KHAMIRUL AMIN MATORI*,**, MOHD HAFIZ MOHD ZAID*,**,
CHE AZURAHANIM CHE ABDULLAH*,**, NORHAZLIN ZAINUDDIN***, IBRAHIM MUSTAPHA ALIBE*,
NADIA ASYIKIN ABDUL RAHMAN**, SITI AISYAH ABDUL WAHAB*

*Material Synthesis and Characterization Laboratory, Institute of Advanced Technology, Universiti Putra Malaysia,
43400 UPM Serdang, Selangor
**Department of Physics, Faculty of Science, Universiti Putra Malaysia,
43400 UPM Serdang, Selangor
***Department of Chemistry, Faculty of Science, Universiti Putra Malaysia,
43400 UPM Serdang, Selangor

#E-mail: khamirul@upm.edu.my

The effect of three different initial alkaline pH values (pH = 8, 9 and 10) in synthesised hydroxyapatite (HA) via a wet chemical precipitation approach was investigated. Waste ark clam shells (ACS) were used in this work as a source of calcium oxide in order to utilise waste materials in the production of synthetic Hydroxyapatite (HA). The HA was treated at different sintering temperature from 200 to 1000 °C to study the effect on the physical, the structural properties, the phase formation, the Vickers microhardness and the molar ratio of calcium to phosphate (Ca:P). From the results, the crystallite size and density of the HA obtained were increased as the sintering temperature increased. However, the appearance of biphasic HA and β-tricalcium phosphate (β-TCP) was detected at pH 9 with 1000 °C, but did not occur at pH 8 and 10. In addition to the obtained results, it was clearly identified that the formation of β-TCP in the HA phase is related to the initial pH value, sintering temperature and Ca:P ratio. The Vickers microhardness showed that the single-phase HA was the hardest one compared to the biphasic HA/β-TCP. It shows the optimal value of the Vickers microhardness for the single-phase HA with a pH 10 at 1000 °C is 4.15 MPa.

INTRODUCTION

Nowadays, the biomedical field is becoming an important sector in the globalization of international health. The biomedical industry tries to create a better synthetic HA due to the high demand around the world. HA with the chemical formulation of $Ca_{10}(PO_4)_6(OH)_2$ is usually found in the main mineral of the hard bone component and teeth [1, 2]. HA is an inorganic compound which is essential in biomedical applications [2-5]. The excellent compatibility of HA in a biological organism, such as a bone implant, has a high impact on orthopaedic applications [6-9]. In addition, the biocompatible and non-toxic properties of HA enable it to be used in the human body as superior biomaterials [10-11]. However, HA is relatively poor in mechanical properties and, thus, is limited its usage in non-load bearing applications [12, 13]. One of the ways to improve this weakness, which can be solved by the addition of other elements such as titanium dioxide (TiO_2), is to use a heat treatment process on the HA sample below 1250 °C [12, 14].

The synthesis of HA from various waste materials has attracted various researchers to investigate the properties of synthetic HA in terms of its biocompatibility and mechanical properties. Waste materials have been used as a source of calcium in the synthesised HA and it has been reported by researchers that it was in order to realise the usability of the waste materials. Sea shells [15-17], egg shells [12, 18, 19], animal bones [20-22] and fruit waste extracts [23] are some examples of the waste materials that are used in research nowadays. These materials are rich in the calcium element and contain other trace elements which are important in the bone tissue engineering field to prepare natural bone [24]. In addition, from the previous reports, the trace elements have been found to play vital roles in the formation, growth and repairing of bones. The addition of trace elements in the calcium phosphate salt such as HA was demonstrated by various studies and offers advantages which can lead to the controlled degradation, increase in the mechanical strength of the materials and provides a positive influence on the biological response [24-27].

The important thing is to ensure the end product is only a single-phase HA by controlling the molar value of the Ca:P ratio and initial alkaline pH value. Koutsopoulos (2002) stated that HA can be synthesised at 1.69 of the Ca:P ratio [28]. When the Ca:P ratio value is lower than 1.69, the deficient calcium in the solution will occur. As a result, the deficient calcium in the synthesis process will produce another calcium phosphate salt such as β-TCP and tetracalcium phosphate (TTCP). Koutsopoulos, (2002) also claimed the different values of the Ca:P ratio may produce different products [28]. The secondary phase of HA, such as calcium hydroxide, was formed when the Ca:P ratio was at 1.69 and above [29]. Thus, the bi-phase of HA/β-TCP will be formed if the Ca:P ratio or the pH value is changed as a parameter.

The synthesis method is one of the roles in producing a single-phase HA. Various methods such as the solid-state method [17], the sol-gel method [3, 30, 31], the hydrothermal method [15, 32] and the wet chemical precipitate method [10, 33, 34] were proposed in the fabrication of HA. However, these conventional methods mostly produce an irregular shape in the particles [32]. The wet chemical precipitate method was used due to its versatility and economic viability. It also promises the HA product to be on a nano-range scale of the particle depending on the parameters, such as the Ca:P ratio, the pH value and temperature.

In this work, the properties of nano-HA were derived from ark clam shells through different initial alkaline pH values and sintering temperatures. The initial pH values play an important role in order to produce a single-phase HA. Thus, several pH values (pH = 8, 9 and 10) and sintering temperatures (200 °C, 600 °C, 800 °C and 1000 °C) were applied to determine the effect of the pH and sintering temperatures on the HA phase product. Both single and secondary phases of HA such as β-TCP is potentially usable for the component synthetics of bone in bio-ceramic materials depending on the specific part in the human body.

EXPERIMENTAL

The raw materials

An ACS was soaked in a water container for a day and cleaned thoroughly from dirt and organic matter. Then, it was dried using an electronic oven at 60 °C for 4 hours. The dried ACS, rich in calcium carbonate ($CaCO_3$), was calcined in the electric furnace (900 °C for 4 hours) to produce a calcium oxide (CaO). After the calcination process, the ACS becomes amorphous and easy to crush by using a plunger and then it can be ground using a mortar and pestle to form a powder. The raw powder was sieved through ≤ 45 μm to form a uniform powder.

Preparation of the calcium hydroxide ($Ca(OH)_2$)

A specific volume of distilled water and CaO powder was mixed together to produce 1.0 M of $Ca(OH)_2$, and then left for 2 hours with a uniform stirring speed of 600 rpm (at room temperature) using a magnetic stirrer. The solution becomes cloudy and white in colour at the end of this process due to some of the undissolved CaO powder directly in the water.

Preparation of the Phosphoric Acid (H_3PO_4)

The titration method was used in producing 0.6M of H_3PO_4 from the pure H_3PO_4. A specific volume for both the pure H_3PO_4 and distilled water was mixed and stirred together to form a homogeneous solution. Finally, 0.6 M of the H_3PO_4 solution was ready to be used.

Preparation of the HA

1.0 M of $Ca(OH)_2$ and 0.6 M of the H_3PO_4 solution was mixed using the titration method to produce an HA precipitation. The H_3PO_4 solution was added drop-wise to the $Ca(OH)_2$ solution at a rate of 15 ml·min^{-1} with continuous stirring which was rotated at the rate of 600 rpm using a magnetic stirrer at room temperature. In this process, the ammonia solution was added in order to maintain the solution at the pH value of 8. Continuous stirring was applied on the solution for 24 hours after the titration process was complete using the same rate of rotation. The solution was left for a while after the 24-hour stirring process. As a result, the solution becomes a two-part layer, where a white gelatinous precipitation was formed. The precipitate was then filtered using a filter paper and washed several times with distilled water before being dried in the oven at 200 °C for 24 hours. The dried HA was ground and sieved into the size of ≤ 45 μm. After that, HA pellets were formed by using a hydraulic press at 2 tonnes of pressure. The diameter of the pellets are 10 mm and 0.5 mm in thickness. The pellets were sintered at temperature of 600 °C to 1000 °C for 4 hours. All the HA pellets were ground using a mortar and pestle to obtain a fine powder for further analysis. These methods were repeated using different initial pH values of 9 and 10 during the HA preparation.

Characterisation of the HA

The structural properties of all the series of samples were analysed using an (XRD) diffractometer (Philips X-ray diffractometer with Cu Kα radiation, λ = 1.5406 Å). The XRD pattern obtained was analysed using the PANalytical X'Pert Pro PW3050/60 diffractometer software at the diffraction angle (2θ) in the scanning range from 20° to 60°. The chemical bonding of the samples was determined using (FTIR) spectroscopy (Perkim

Elmer Spectrum 100 series). The FTIR spectra were recorded at room temperature between 280 and 4000 cm^{-1}. The physical properties of the HA, such as crystallite size, linear shrinkage, and density are recorded. The crystallite size of the sample was measured using Debye-Scherrer's Equation by XRD High Score Plus software. The densities of the HA sintered material were determined using an Archimedes method which uses ethanol as the immersion liquid. Furthermore, the hardness of the HA was determined by using a Vickers microhardness (H_v) machine. The Vickers microhardness is used to measure the mechanical hardness of the HA. The sample was tested at a fixed 0.3 g F load with a 15 second dwell time. The microstructure and morphology of the samples were observed by using field emission scanning electron microscopy (FESEM), (FEI NOVA NanoSEM 230) with a magnification of 50K. The elements of the sample were analysed by energy dispersive X-ray spectroscopy (EDX) with the same model of FESEM.

RESULT AND DISCUSSION

$CaCO_3$ can form in three different polymorphic minerals which are known as calcite, aragonite and vaterite [35-36]. In Figure 1, the raw ACS, which contains $CaCO_3$, appeared in the form of calcite and aragonite from the XRD results. This result was similar to the results obtained by Loy and co-workers who studied the element composition of ACS [35]. The calcite and aragonite have same chemical formula which is $CaCO_3$, but have a different crystalline structure. Besides that, calcite is trigonal while aragonite is orthorhombic in the
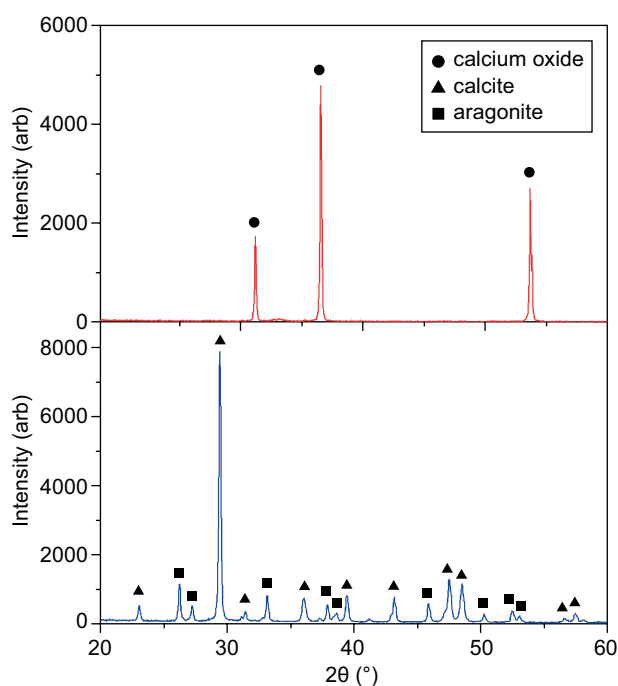
crystal system. The raw ACS showed that the single-phase $CaCO_3$ decomposed into the CaO phase after the calcination process. From the XRD pattern in Figure 1a, it can be seen that the $CaCO_3$ phase from the ACS is in the form of a different crystalline structure which indicates the peaks of calcite (JCPDS: 00-005-0586) and aragonite (JCPDS: 00-005-0453). The $CaCO_3$ phase of calcite and aragonite decomposed to the CaO phase by releasing carbon dioxide (CO_2) during the calcination process at 900 °C for 4 hours as shown in Equation 1. It can be observed that the presence of three peaks exist from the XRD pattern in Figure 1b which represents the CaO phase (JCPDS: 00-037-1497). Previous research reported the decomposition of the $CaCO_3$ to CaO phase started to occur at a temperature between 800 °C and 1000 °C [13, 35, 37-38].

$$CaCO_3 \,(s) \rightarrow CaO \,(s) + CO_2 \,(g) \qquad (1)$$
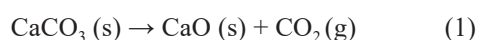
The powder obtained at the initial pH value of 8 was analysed and confirmed as the HA powder which matches with JCPDS: 00-009-0432. Chemical Equation 2 shows the reaction of the $Ca(OH)_2$ and H_3PO_4 solution to produce HA and water. The reaction was controlled with the Ca:P ratio at 1.67 based on Equation 2. The HA powder was sintered at a temperature of 600 °C, 800 °C and 1000 °C. Figure 2 shows the XRD pattern of the HA with the different sintering temperatures at a pH value of 8. From the XRD analysis, as the sintering temperature increases, the intensity increases and becomes sharper. It became more obvious at 1000 °C due to migration of the crystal boundaries with the increment of the sintering temperature. The HA peak is a match with the reference as shown in Figure 2 and it can be seen in the XRD pattern in Figure 2 that it does not show a noticeable peak of β-TCP.

$$10Ca(OH)_2 \,(aq) + 6H_3PO_4 \,(aq) \rightarrow$$
$$\rightarrow Ca_{10}(PO_4)_6(OH)_2(s) + 18H_2O \,(aq) \qquad (2)$$
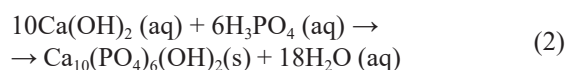
As the pH value increase to 9, the XRD pattern shows no differences with the as-synthesised HA powder that is same as the XRD pattern of the initial pH value at 8. However, as the sintering temperature increases to 800 °C, the XRD patterns start to indicate the main peak of β-TCP at a position of 2θ = 31.1°. The XRD pattern in Figure 2 become obvious at 1000 °C which is indicated by the peak of β-TCP becoming sharper. The bi-phase of the HA/β-TCP composition occurs due to the decomposition of some of the HA to the β-TCP phase which is same as reported in other research [4, 13, 38]. The decomposition of the partial HA is related to the changes of the Ca:P ratio values due to deficiency of calcium, phosphate or both of these elements in the sample at high temperatures.

Figure 2 also shows the XRD pattern of the HA with the initial pH value of 10 and it was observed that it has an exactly the same XRD pattern as compared to the initial results of the pH of 8 from 200 °C to 1000 °C.

Figure 1. The XRD pattern of: a) the raw ACS and b) CaO after calcination at 900 °C for 4 hours.

However, the peak intensity of HA for the pH value of 10 is higher than the pH value of 8. It shows the crystallinity of HA for a pH of 10 is better compared to that of a pH of 8. Besides that, the dehydroxylation of the HA structure occurs as the sintering temperature increases up to 1000 °C. Equation 3 shows the dehydroxylation of HA occurs for all pH values. The decomposition of HA to β-TCP was detected after the sintering process at higher temperature [13, 33, 34]. In this work, the phase of β-TCP only appeared at a pH of 9 and the single-phase of HA was present for both the pH of 8 and 10. However, the phase of β-TCP for both the pH of 8 and 10 are expected to appear at 1000 °C and above, the same as previous research [13, 33]. Thus, the formation of β-TCP cannot be observed at a sintering temperature lower than 1000 °C depending on the pH values and the Ca:P ratio [38].

$$Ca_{10}(PO_4)_6(OH)_2(s) \rightarrow$$
$$\rightarrow Ca_{10}(PO_4)_6(OH)_{2-2x}O_x(s) + xH_2O \text{ (aq)} \qquad (3)$$
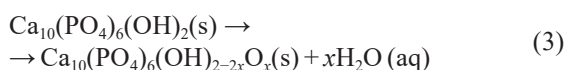
The chemical bonding of the raw ACS before and after the calcination process in the electric furnace is shown in Figure 3. The FTIR spectrum was scanned in the frequency range of 280 - 4000 cm^{-1}. The raw ACS which is rich in $CaCO_3$ was indicated from the infrared absorption spectra at peak of ~705 cm^{-1}, ~855 cm^{-1}, ~1082 cm^{-1}, ~1454 cm^{-1}, ~1786 cm^{-1} and ~2520 cm^{-1} [13, 38]. These peaks refer to the carbonated ion group that is present in the raw ACS. At the band of ~855 cm^{-1}, it was fully assigned to the symmetric stretching mode, v_1, while the band of ~1082 was assigned to the out-of-plane bending mode, v_2, of the CO_3^{2-} ion in the raw ACS. In addition, the spectra of ~1082 cm^{-1} only can be found in the spectrum of the aragonite phase of the calcium carbonate which shows a small peak in the infrared region. A similar observation was reported previously by the researcher who studied the infrared band of the calcium carbonate which focuses on the aragonite phase [39]. However, the ACS consists of both an aragonite and calcite phase as verified by the XRD result. The peak at ~705 cm^{-1} in the infrared spectra verified the CO_3^{2-} ion which is in the in-plane bending mode, v_4, that was found in the spectrum of the calcite phase of calcium carbonate, which is more active than the aragonite phase. The spectra at ~1454 cm^{-1} indicated the structure of the asymmetric stretching mode, v_3, of the CO_3^{2-} molecular ion of calcite. This result was supported by Cheng et al. (2010) [40]. The frequencies at ~1786 cm^{-1} and ~2520 cm^{-1} are present from the combination of the fundamental vibration frequencies of the carbonate molecular ion which was identified between (v_1 and v_4) and (v_1 and v_3), respectively. This observation agrees with the previous reported research [39, 40, 41]. The stretching vibration of the hydroxyl group was found at the spectra of ~3743 cm^{-1}.

The FTIR spectrum of the raw ACS after the calcination process shows three different small peaks of spectrum at ~1456 cm^{-1}, ~3480 cm^{-1} and ~3742 cm^{-1}. These peaks of frequency were indicated by the structure of CaO after being exposed to the calcined process for 4 hours at 900 °C in the electrical furnace. The infrared band at ~1456 cm^{-1} describes the presence of the Ca–O bond in CaO. This peak was also verified by other research, which studied the formation of the CaO phase from $CaCO_3$ at different calcined temperature [35]. The decomposition of CO_2 from $CaCO_3$ by a calcination process was verified by the XRD pattern in this study. However, the characteristic of CaO has a high hydro adsorption strength compared to $CaCO_3$ due to it being
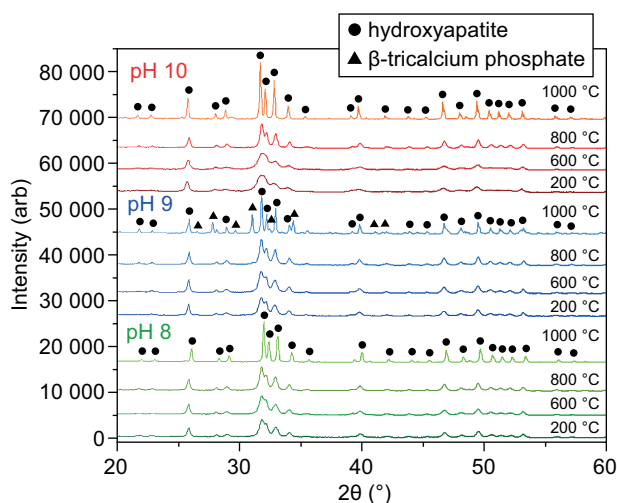

Figure 2. Shows the HA powder from the initial pH value of 8, 9 and 10 at the different sintering temperatures from 200 to 1000 °C for 4 hours.
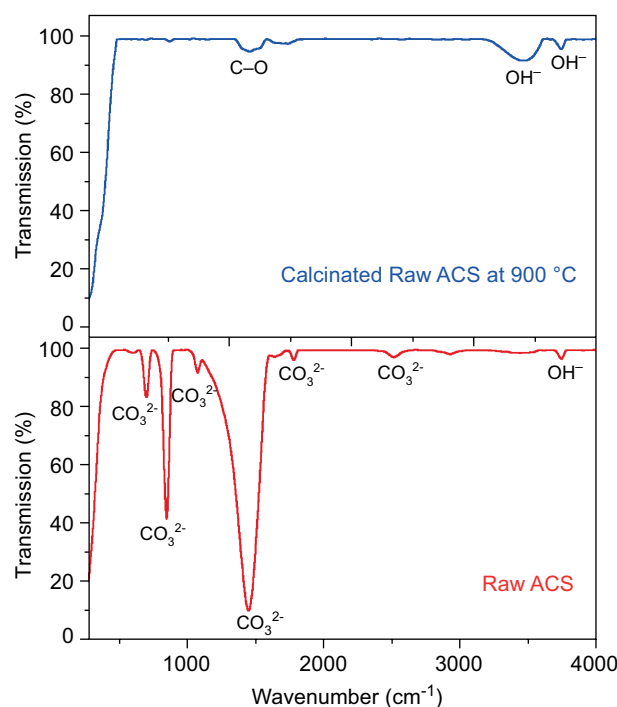

Figure 3. The FTIR spectrum of the raw ACS and calcined ACS at 900 °C for 4 hours in the electric furnace.

more polar in CaO rather than CaCO$_3$. As a result, CaO is easily becomes attracted to the water molecule in the form of moisture to form aCa-OH bond in Ca(OH)$_2$. The band at ~3480 cm^{-1} and ~3742 cm^{-1} were related to the OH$^-$ bond group in CaO. Table 1 shows the summary of the vibration mode of the ACS and the calcinated ACS at 900 °C.

Table 1. The vibration mode of the ACS and calcinated ACS.

Raw ACS	
Bonding mode	Vibrational frequency (cm^{-1})
v_4 Symmetric CO$_3^{2-}$ deformation	708
v_2 Asymmetric CO$_3^{2-}$ deformation	855
Symmetric stretching vibration CO$_3^{2-}$	1082
v_3 Asymmetric CO$_3^{2-}$ deformation	1454
v_1 + v4 CO$_3^{2-}$ deformation	1786
v_1 + v4 CO$_3^{2-}$ deformation	2520
OH$^-$ stretching mode	3743
Calcinated ACS at 900 °C	
Bonding mode	Vibrational frequency (cm^{-1})
Ca–O	1456
OH$^-$ stretching mode	3480, 3742

Figure 4 shows the infrared spectrum of the HA at the initial pH value of 8 for various sintering temperatures from 200 °C to 1000 °C. The infrared absorption spectrum was scanned from 280 cm^{-1} to 4000 cm^{-1}. From the result, the frequency bands at ~565 cm^{-1} and 1024 cm^{-1} correspond to the PO$_4^{3-}$ group. The bending structure, v_3 of PO$_4^{3-}$ and v_4 of PO$_4^{3-}$ were observed at ~1024 cm^{-1} and ~565 cm^{-1}, respectively. A similar result was reported previously by several researchers [13, 42].
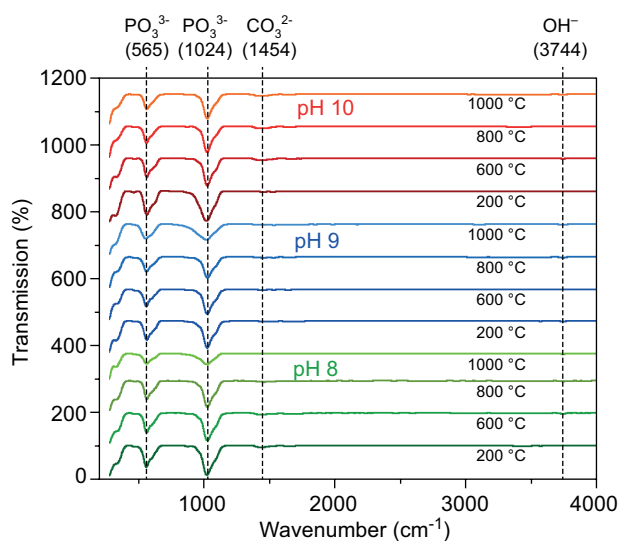

Figure 4. The FTIR spectrum of the HA at the initial pH value of 8, 9 and 10 with different sintering temperatures from 200 to 1000 °C.

From Figure 4, the peak of the bending structure for both v_3 and v_4 decreased as the sintering temperature increased due to the decomposition of some of the HA to a β-TCP phase. Meanwhile, the CO$_3^{2-}$ vibration band mode, v_3 was detected at ~1454 cm^{-1} in the as-synthesised HA. This CO$_3^{2-}$ vibration band mode, v_3 was detected due to the presence of the carbonate substitute with the PO$_3^{2-}$ ion in the HA lattice [13]. However, this band is no longer visible when the sintering temperatures increase up to 1000 °C. A similar result was reported by Kamalanathan et al (2014), due to elimination of CO$_3^{2-}$ at the elevated temperature [13]. The band at ~3744 cm^{-1} was observed in the HA infrared spectrum due to the stretching mode of the hydrogen-bonded OH$^-$ ion [42]. There are no obvious differences shown in the infrared absorption spectrum for the HA at the pH values of 8, 9 and 10. Table 2 shows the summary of the chemical bonding for HA.

Table 2. The FTIR frequencies of HA.

Assignments	Frequency (cm^{-1})
PO$_3^{3-}$ bend $v4$	~565
PO$_3^{3-}$ bend $v3$	~1024
CO$_3^{2-}$ group $v3$	~1454
OH$^-$ structure	~3744

The physical properties of HA were measured in terms of the crystallite size, the linear shrinkage and density with the different sintering temperatures and initial pH values shown in Table 2. From the table, the crystallite size of HA increases as the sintering temperature increases from 200 °C to 1000 °C for all pH value. The crystallite size of the as-synthesized HA for all pH values was calculated between ~26.58 and 29.53 nm. As the sintering temperature increases to 1000 °C, the crystallite size of the HA also increases and reached up to ~53.18 nm. Furthermore, the linear shrinkage shows an increment when the sintering temperature increases. This occurs when the crystallite size increased proportionally to the sintering temperature and eliminates the porosity in the sample [2, 43]. As a result, the density of the HA also increased as the temperature increased [22]. In Table 3, the density increases from 200 °C to 1000 °C followed by the Vickers microhardness in Table 4. However, in Table 3, the density increases from 200 °C to 800 °C and then slightly decreases when it reaches 1000 °C. This is due to the decomposition of some HA to β-TCP at the high sintering temperature. Kamalanathan et al. (2014) state that the decrease in the density of the sample ascribed the presence of other TCP phases which are secondary phases of β-TCP and α-TCP [13]. This result was similar to previous reports where they studied the behaviour of HA at high sintering temperature [8, 13, 44, 45].

The Vickers microhardness of the HA samples were measured by taking 5 different indentations on the flattened and smooth surface. All the samples must be

Table 3. The crystallite size, linear shrinkage and density of the HA at various sintering temperature with the initial pH values of 8, 9 and 10.

pH value	Temperature (°C)	Crystallite size, D (nm)	Linear shrinkage (%)	Density (g·cm^{-3})
8	200	26.58	0	2.76
	600	29.54	3.08	2.81
	800	37.89	6.15	2.95
	1000	53.18	11.53	3.10
9	200	29.53	0	2.86
	600	31.74	2.81	3.12
	800	37.97	5.53	3.01
	1000	53.15	9.71	2.87
10	200	26.59	0	2.89
	600	33.26	2.41	3.04
	800	37.98	3.23	3.12
	1000	53.16	10.12	3.17

polished before testing by the Vickers microhardness measurement and the measurements are fixed at a 0.3 gF load with a 15 second dwell time. In this measurement, the Vickers microhardness of the HA samples with different pH values (8, 9 and 10) sintered at 200 to 1000 °C were measured and tabulated in Table 4. The hardness of the HA sample for all the pH values of 8, 9 and 10 increased as the sintering temperatures rose from 200 to 1000 °C. It was observed that the maximum value of hardness is 1.47, 1.19 and 4.15 GPa at 1000 °C for each of the different pH values as shown in Figure 5, respectively. From the results, it can also be seen that the HA samples at the pH value of 10 show the highest hardness compared to the other pH values (8 and 9). It is might be related to the high phase stability of the HA at the pH of 10 compared to the lower pH values. Furthermore, the trend of the hardness increased as the sintering temperature increased and these results followed the general trend of hardness against temperature. By comparing with the density of the sample, it has the same pattern as the hardness measurement where both the density and hardness increased as the sintering temperature increased. The increases in the hardness measurement for the obtained HA sample is in good agreement with the other reported work [13, 22, 43]. Besides that, the increases in the hardness are related to the increases in the linear shrinkage and density of the HA. This can be

proven by the densification of the HA when the sintering temperature was increased. In this stage, the samples tend to be more compact and eliminate the porosity. Butkovic et al. (2012) stated the high sintering temperature can cause the atomic diffusion to exhibit more intensively [46]. Thus, the crystal boundaries in the sample were migrating faster and form a denser material. As a result, the hardness of the HA becomes tougher and harder.

The FESEM micrograph in Figure 6 showed the difference in the sintering temperature under the specific

Figure 5. The Vickers microhardness of the HA with a pH value of 8, 9 and 10 with various sintering temperatures.

Table 4. The Vickers microhardness of the different pH values with various sintering temperatures.

Temperature (°C)	Hardness, H_v (GPa)		
	Initial pH value of HA		
	pH = 8	pH = 9	pH = 10
200	0.48	0.46	0.35
600	0.53	0.47	0.59
800	0.75	0.84	0.80
1000	1.47	1.19	4.15

pH = 8   pH = 9   pH = 10

Sintering temperature: 200 °C

pH = 8   pH = 9   pH = 10

Sintering temperature: 600 °C

pH = 8   pH = 9   pH = 10

Sintering temperature: 800 °C

pH = 8   pH = 9   pH = 10
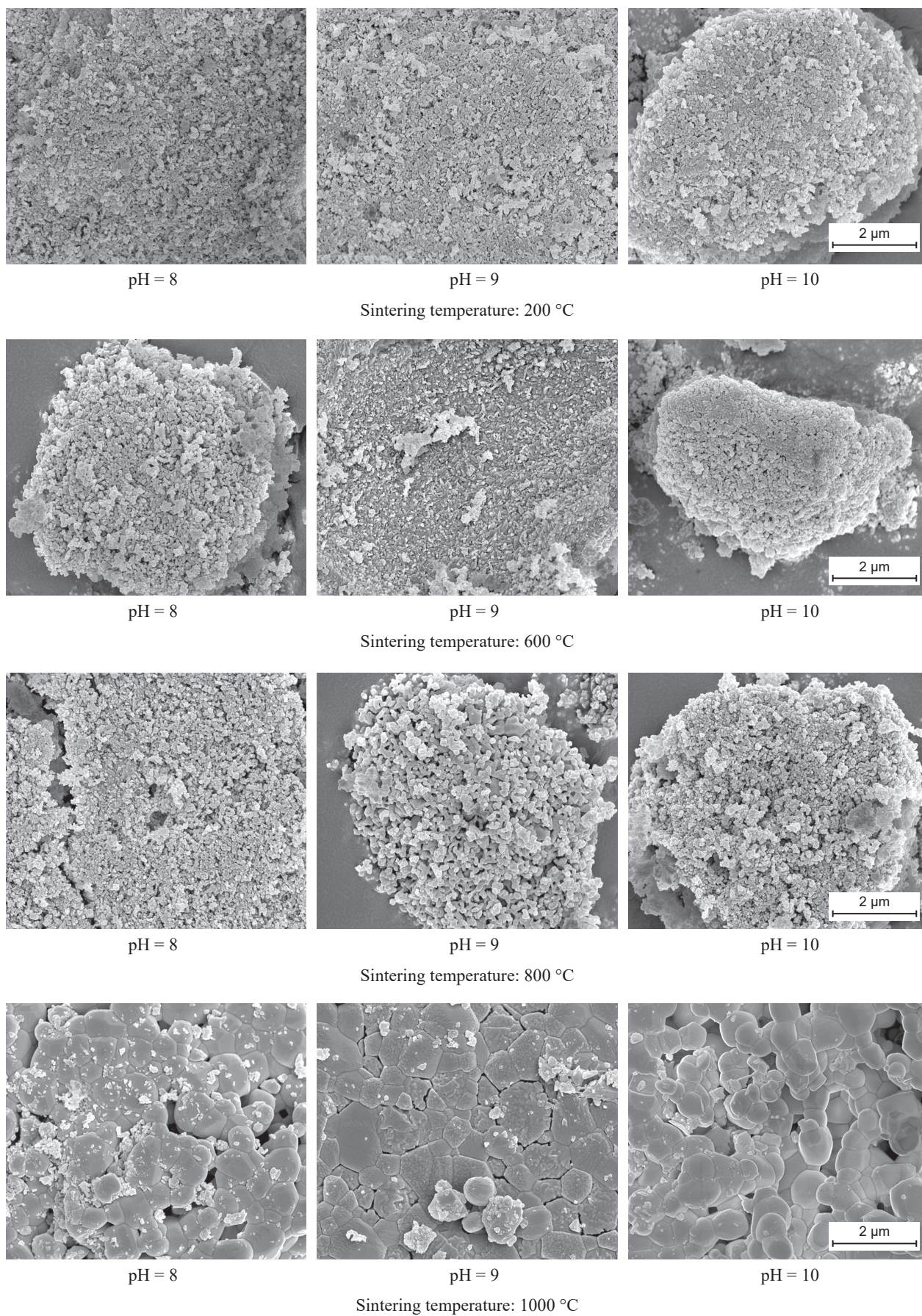
Sintering temperature: 1000 °C

Figure 6. The FESEM morphology of the HA with the initial pH value of 8, 9 and 10 at various sintering temperatures.

initial pH values of the HA. From the FESEM micrograph, the morphology of the HA was not obviously increasing in size at a temperature between 200 °C and 800 °C for all the initial pH values of 8, 9 and 10. At the initial stage of the temperatures, the HA particle was irregular in shape and mostly showed an agglomerated microstructure. This type of HA morphology was similar with previous reports which were agglomerated and irregular in shape [1, 21, 22]. In addition, from the FESEM micrograph, the average sizes of the particles were measured between ~30 - 70 nm for the as-synthesised at 200 °C. However, as the sintering temperature increases up to 1000 °C, the morphology of the HA sample was obviously increasing in grain size too, where the measured value of the grain size is taken between ~0.30 - 0.80 μm. The grain size becomes more solid in shape and the porosity decreases. It has been found that the advancement in the sintering process leads to an increase in the grain size and a decrease in the porosity for all the initial pH values as shown in Figure 6.

The EDX analysis was carried out to determine the element composition in the HA sample with the different initial pH values. In Table 5, the EDX result shows the elements of Ca, P, O, and C for all the initial alkaline pH values of HA. At a pH value of 8, the value of the Ca:P ratio was calculated at 1.95. This value is slightly higher than the theoretical value which is 1.69. This similar situation was also observed at the pH values of 9 and 10 which was recorded at 2.16 and 2.10, respectively. The different values of the Ca:P ratio between pH 8 and 10 might be related with the alkalinity of the HA solution produced at the initial stage of the synthesised HA or inconsistencies with the calcium element content in the raw ACS. Thus, it is also can affect the homogeneous reaction of the calcium oxide and phosphoric acid to form the HA product at early stages of synthesisation.

Table 5. The weight composition of the HA at the different initial pH values of 8, 9 and 10.

Elements	Weight Composition (wt. %)		
	pH = 8	pH = 9	pH = 10
Ca	25.64	35.16	26.89
P	13.12	16.22	12.77
O	43.76	35.05	46.27
C	17.64	12.56	14.08
Ca:P ratio	1.95	2.16	2.10

CONCLUSIONS

In this present work, nano-HA can be successfully prepared through various initial alkaline pH values with high purities by a simple wet chemical precipitate method. The different initial pH values in the synthesised HA from waste materials provide a high impact on the composition of the HA at higher sintering temperatures, especially at 1000 °C. At this temperature, the β-TCP started to appear in the HA phase at the initial pH value of 9 by comparing the XRD results. The decomposition of HA to β-TCP only occurred at a pH value of 9 (1000 °C) and did not appear at the pH values of 8 and 10. Thus, only a single-phase HA was detected at a pH of 8 and 10. Besides that, all the HA samples consist of PO_4^{2-}, CO_3^{2-}, and OH^- chemical groups as reported in the FTIR results, even though it is prepared with different pH conditions. Moreover, the crystallite size, linear linkage, density and hardness of the sample increases proportionally as the sintering temperature increases for all the HA samples. Next, from the FESEM results, all the HA samples show an agglomerated condition, are irregular in shape and increase in size as the sintering temperature increases. The porosity of the samples also decreased as the sintering temperatures increased, hence giving a positive result in the Vickers microhardness. The HA with a single-phase is harder when compared to the biphasic HA/β-TCP. From the results, it can be observed that the optimal value for the single-phase HA with a pH of 10 at 1000 °C is 4.15 MPa. However, the EDX result in this work shows an inconsistent value as the pH value changes from 8 to 10. As a conclusion, the pH values and sintering temperatures are very important parameters in producing HA since it will effect the phase conditions of the HA.

REFERENCE

1. Mostafa N.Y. (2005): Characterization, thermal stability and sintering of hydroxyapatite powders prepared by different routes. *Material Chemistry Physics*, 94, 333-341. doi: 10.1016/j.matchemphys.2005.05.011
2. Abidi S.S.A., Murtaza Q. (2014): Synthesis and characterization of nano-hydroxyapatite powder using wet chemical precipitation reaction. *Journal of Material Science & Technology*, 30, 307-310. doi: 10.1016/j.jmst.2013.10.011
3. Agrawal K., Singh G., Puri D., Prakash S. (2011): Synthesis and characterization of hydroxyapatite powder by sol-gel method for biomedical application. *Journal of Minerals & Materials Characterization & Engineering*, 10, 727-734.
4. Singh A., Purohit K.M. (2010): Chemical synthesis, characterization and bioactivity evaluation of hydroxyapatite prepared from garden snail (helix aspersa). *Journals of Biotechnology & Biomaterials*, 1, 104-108.

5. Hoque M.E., Sakinah N., Chuan Y.L., Ansari M. (2014): Synthesis and characterization of hydroxyapatite bioceramic. *International Journal of Scientific Engineering and Technology*, 3, 458-462. doi: 10.1186/s40064-016-2824-y

6. Currey J. (2001): Biomaterials: sacrificial bonds heal bone. *Nature*, 414, 699-699. doi: 10.1038/414699a

`7. Kwon S.H., Jun Y.K., Hong S.H., Kim H.E. (2003): Synthesis and dissolution behavior of β-TCP and HA/β-TCP composite powders. *Journal of the European Ceramic Society*, 23 1039-1045. doi: 10.1016/S0955-2219(02)00263-7

8. Cho J.S., Kang Y.C. (2008): Nano-sized hydroxyapatite powders prepared by flame spray pyrolysis. *Journal of Alloys and Compounds*, 464, 282-287. doi: 10.1016/j.jallcom.2007.09.092

9. Hung I., Shih W.J., Hon M.H., Wang M.C. (2012): The properties of sintered calcium phosphate with [Ca]/[P]= 1.50. *International Journal of Molecular Sciences*, 13, 13569-13586. doi: 10.3390/ijms131013569

10. Rujitanapanich S., Kumpapan P., Wanjanoi P. (2014): Synthesis of hydroxyapatite from oyster shell via precipitation. *Energy Procedia*, 56, 112-117. doi: 10.1016/j.egypro.2014.07.138

11. Fathi M.H., Hanifi A., Mortazavi V., (2008): Preparation and bioactivity evaluation of bone-like hydroxyapatite nanopowder. *Journal of Material Processing Technology*, 202, 536-542. doi: 10.1016/j.jmatprotec.2007.10.004

12. Mazaheri M., Haghighatzadeh M., Zahedi A.M., Sadrnezhaad S.K. (2009): Effect of a novel sintering process on mechanical properties of hydroxyapatite ceramics. *Journal of Alloys and Compounds*, 471, 180-184. doi: 10.1016/j.jallcom.2008.03.066

13. Kamalanathan P., Ramesh S., Bang L.T., Niakan A., Tan C.Y., Purbolaksono J., Chandran H., Teng W.D. (2014): Synthesis and sintering of hydroxyapatite derived from eggshells as a calcium precursor. *Ceramic International*, 40, 16349-16359. doi: 10.1016/j.ceramint.2014.07.074

14. Wakily H., Dabbagh A., Abdullah H., Halim N.F.A., Kasim N.H.A. (2015): Improved thermal and mechanical properties in hydroxyapatite–titanium composites by incorporating silica-coated titanium. *Materials Letters*, 143, 322-325. doi: 10.1016/j.matlet.2014.12.092

15. Zhang X., Vecchio K.S. (2006): Creation of dense hydroxyapatite (synthetic bone) by hydrothermal conversion of seashells. *Materials Science & Engineering C*, 26, 1445-1450. doi: 10.1016/j.msec.2005.08.007

16. Kamba A.S., Ismail M., Ibrahim T.A.T., Zakaria Z.A.B. (2013): Synthesis and characterisation of calcium carbonate aragonite nanocrystals from cockle shell powder (Anadara granosa). *Journal of Nanomaterials*, 5, 1-9. doi: 10.1155/2013/398357

17. Chen J., Wen Z., Zhong S., Wang Z., Wu J., Zhang Q. (2015): Synthesis of hydroxyapatite nanorods from abalone shells via hydrothermal solid-state conversion. *Materials & Design*, 87, 445-449. doi: 10.1016/j.matdes.2015.08.056

18. Dávila J.A., Cuevas J.L, Gutiérrez G.V., Angeles J.R., Nonell J.M. (2007): Chemical synthesis of bone-like carbonate hydroxyapatite from hen eggshells and its characterization. *Boletín de la Sociedad Española de Cerámica y Vidrio*, 46, 225-231.

19. Gergely G., Wéber F., Lukács I., Tóth A.L., Horváth Z.E., Mihály J., Balázsi C. (2010): Preparation and characterization of hydroxyapatite from eggshell. *Ceramic International*, 36, 803-806. doi: 10.1016/j.ceramint.2009.09.020

20. Sobczak A., Kowalski Z., Wzorek Z. (2009): Preparation of hydroxyapatite from animal bones. *Acta Bioengineering and Biomechanicals*, 11, 23-28.

21. Venkatesan J., Kim S.K. (2010): Effect of temperature on isolation and characterization of hydroxyapatite from tuna (Thunnus obesus) bone. *Materials*, 3, 4761-4772. doi: 10.3390/ma3104761

22. Niakan A., Ramesh S., Ganesan P., Tan C.Y., Purbolaksono J., Chandran H., Teng W.D. (2015): Sintering behaviour of natural porous hydroxyapatite derived from bovine bone. *Ceramic International*, 41, 3024-3029. doi: 10.1016/j.ceramint.2014.10.138

23. Wu S.C., Tsou H.K., Hsu H.C., Hsu S.K., Liou S.P, Ho W.F. (2013): A hydrothermal synthesis of eggshell and fruit waste extract to produce nanosized hydroxyapatite. *Ceramic International*, 39, 8183-8188. doi: 10.1016/j.ceramint.2013.03.094

24. Bose S., Fielding G., Tarafder S., Bandyopadhyay A. (2013): Trace element doping in calcium phosphate ceramics to understand osteogenesis and angiogenesis. *Trends Biotechnology*, 31, 1-10. doi: 10.1016/j.tibtech.2013.06.005

25. Bohner M. (2009): Silicon-substituted calcium phosphates–a critical view. *Biomaterials*, 30, 6403-6406. doi: 10.1016/j.biomaterials.2009.08.007

26. Li X., Sogo Y., Ito A., Mutsuzaki H., Ochiai N., Kobayashi T., Nakamura S., Yamashita K., LeGeros R.Z. (2009): The optimum zinc content in set calcium phosphate cement for promoting bone formation in vivo. *Materials Science & Engineering C*, 29, 969-975. doi: 10.1016/j.msec.2008.08.021

27. Fielding G.A., Bandyopadhyay A., Bose S. (2012): Effects of silica and zinc oxide doping on mechanical and biological properties of 3D printed tricalcium phosphate tissue engineering scaffolds. *Dental Materials*, 28, 113-122. doi: 10.1016/j.dental.2011.09.010

28. Koutsopoulos S. (2002): Synthesis and characterization of hydroxyapatite crystals: a review study on the analytical methods. *Journal of Biomedical Research*, 62, 600-612. doi: 10.1002/jbm.10280

29. Ansari M., Naghib S.M., Moztarzadeh F., Salati A. (2011): Synthesis and characterisation of hydroxyapatite-calcium hydroxide for dental. *Ceramic Silikaty*, 55, 123-126.

30. Sanosh K.P., Chu M.C., Balakrishnan A., Kim T.N., Cho S.J. (2009): Preparation and characterization of nano-hydroxyapatite powder using sol-gel technique. *Bulletin of Materials Science*, 32, 465-470. doi: 10.1007/s12034-009-0069-x

31. Anitha P., Pandya H.M. (2014): Synthesis, characterization and antimicrobial activity of nano hydroxyapatite via a novel sol gel method. *Nano Technology Research Practice*, 3, 120-126. doi: 10.13187/ejnr.2014.3.120

32. Zhu R., Yu R., Yao J., Wang D., Ke J. (2008): Morphology control of hydroxyapatite through hydrothermal process. *Journal of Alloys & Compounds*, 457, 555-559. doi: 10.1016/j.jallcom.2007.03.081

33. Mobasherpour I., Heshajin M.S., Kazemzadeh A., Zakeri M. (2007): Synthesis of nanocrystalline hydroxyapatite by using precipitation method. *Journal of Alloys & Compounds*, 430, 330-333. doi: 10.1016/j.jallcom.2006.05.018

34. Tahriri M., Solati-Hashjin M., Eslami H. (2008): Synthesis and characterization of hydroxyapatite nanocrystals via chemical precipitation technique. *Iranian Journal of Pharmaceutical Sciences*, 4, 127-134.

35. Loy C.W., Matori K.A., Lim W.F., Schmid S., Zainuddin N., Wahab Z.A., Zaid M.H.M. (2016): Effects of calcination on the crystallography and nonbiogenic aragonite formation of ark clam shell under ambient condition. *Advances in Materials Science and Engineering*, 1-8. doi: 10.1155/2016/2914368

36. Islam K.N., Bakar M.Z.B.A., Noordin M.M., Hussein M.Z.B., Rahman N.S.B.A., Ali M.E. (2011): Characterisation of calcium carbonate and its polymorphs from cockle shells (Anadara granosa). *Powder Technology*, 213, 188-191. doi: 10.1016/j.powtec.2011.07.031

37. Singh A. (2012): Hydroxyapatite, a biomaterial: Its chemical synthesis, characterization and study of biocompatibility prepared from shell of garden snail, Helix aspersa. *Bulletin of Materials Science*, 35, 1031-1038. doi: 10.1007/s12034-012-0384-5

38. Khiri M.Z.A., Matori K.A., Zainuddin N., Abdullah C.A.C., Alassan Z.N., Baharuddin N.F., Zaid M.H.M. (2016): The usability of ark clam shell (Anadara granosa) as calcium precursor to produce hydroxyapatite nanoparticle via wet chemical precipitate method in various sintering temperature. *SpringerPlus*, 5, 1206-1221. doi: 10.1186/s40064-016-2824-y

39. Raju C.L., Narasimhulu K.V., Gopal N.O., Rao J.L., Reddy B.C.V. (2002): Electron paramagnetic resonance, optical and infrared spectral studies on the marine mussel Arcaburnesi shells. *Journal of Molecular Structure*, 608, 201-211. doi: 10.1016/S0022-2860(01)00952-8

40. Cheng B., Cai W., Yu J. (2010): DNA-mediated morphosynthesis of calcium carbonate particles. *Journal of Colloid and Interface Science*, 352, 43-49. doi: 10.1016/j.jcis.2010.08.050

41. Vongsavat V., Winotai P., Meejoo S. (2006): Phase transitions of natural corals monitored by ESR spectroscopy. *Nuclear Instruments and Methods in Physics Research Section B: Beam Interactions with Materials and Atoms*, 243, 167-173. doi: 10.1016/j.nimb.2005.07.197

42. Eslami H., Tahriri M., Bakhshi F. (2010): Synthesis and characterization of nanocrystalline hydroxyapatite obtained by the wet chemical technique. *Material Science Poland*, 28, 5-13.

43. Yeong K.C.B., Wang J., Ng S.C. (2001): Mechanochemical synthesis of nanocrystalline hydroxyapatite from CaO and $CaHPO_4$. *Biomaterials*, 22, 2705-2712. doi: 10.1016/S0142-9612(00)00257-X

44. Aminzare M., Eskandari A., Baroonian M.H., Berenov A., Hesabi Z.R., Taheri M., Sadrnezhaad S.K. (2013): Hydroxyapatite nanocomposites: Synthesis, sintering and mechanical properties. *Ceramic International*, 39, 2197-2206. doi: 10.1016/j.ceramint.2012.09.023

45. Zilm M., Thomson S.D., Wei M. (2015): A comparative study of the sintering behavior of pure and manganese-substituted hydroxyapatite. *Materials*, 8, 6419-6436. doi: 10.3390/ma8095308

46. Butkovic S., Oruc M., Saric E., Mehmedovic M. (2012): Effect of sintering parameters on the density, microstructure and mechanical properties of the niobium-modified heat-resistant stainless steel GX40CrNiSi25-20 produced by MIM technology. *Materiali in Technologije*, 46, 185-190.